PERGAMON

International Journal of Heat and Mass Transfer 44 (2001) 537–550

International Journal of HEAT and MASS TRANSFER

www.elsevier.com/locate/ijhmt

Low-Prandtl number natural convection in volumetrically heated rectangular enclosures II. Square cavity, $AR = 1$

Salvatore Arcidiacono, Ivan Di Piazza, Michele Ciofalo*

Dipartimento di Ingegneria Nucleare, Università di Palermo, Viale delle Scienze, 90128 Palermo, Italy

Received 7 January 2000; received in revised form 22 March 2000

Abstract

Following a previous study for a slender enclosure ($AR = 4$), direct numerical two-dimensional simulations were conducted for the free convective flow of a low-Prandtl number fluid ($Pr = 0.0321$) with internal heat generation in a square cavity having adiabatic top and bottom walls and isothermal side walls. The Grashof number, Gr, based on conductive maximum temperature and cavity width, ranged from 10^5 to 10^9. For Gr up to $\sim 10^7$, the flow was steady and exhibited left–right symmetry. For $Gr \approx 3 \times 10^7$, the spatial symmetry was broken and asymmetric steady-state flow patterns were obtained. For $Gr \approx 5 \times 10^7$, the asymmetric flow became time-periodic. Finally, for $Gr \geq 10^8$, chaotic flow was predicted; the time-averaged velocity and temperature fields were still markedly asymmetric at $Gr = 10^8$, but reattained bilateral symmetry at higher Gr (10^9), when developed two-dimensional turbulence was observed. For Grashof numbers above $\sim 10^6$, the friction coefficient averaged along the vertical walls scaled roughly with $Gr^{-1/3}$ (as in the $AR = 4$ cavity), while the Nusselt number (overall/conductive heat transfer) increased roughly as $Gr^{1/7}$, i.e. slightly less markedly than in the slender cavity.

1. Introduction and previous work

As discussed in Ref. [1], studies of free convection in enclosures with internal heat generation have been conducted for some considerable time in connection with geophysical [2] or nuclear [3] applications, and have usually focussed on shallow cavities and large Prandtl numbers. More recently, the problem of free convection with volumetric heat sources has represented itself in connection with advanced engineering applications, such as water-cooled lithium–lead breeder blankets for nuclear fusion reactors [4] and liquid metal sources of spallation neutrons for subcritical fission systems [5]. In these applications, the Prandtl number is usually small (liquid metals) and additional effects, such as magnetohydrodynamic interactions, may play a role.

In a previous paper [1], direct numerical two-dimensional simulations were reported for the natural convection flow in a volumetrically heated slender rectangular enclosure filled with a low-Prandtl number fluid ($Pr = 0.0321$). The enclosure had isothermal side walls and adiabatic top/bottom walls. The aspect ratio Ar was 4 and the Grashof number Gr, based on conductive maximum temperature and cavity width, ranged from 3.79×10^4 to 1.26×10^9.

* Corresponding author. Tel.: +39-091-232-257; fax: +39-091-232-215.

E-mail address: ciofalo@din.din.unipa.it (M. Ciofalo).

0017-9310/01/$ - see front matter
PII: S0017-9310(00)00118-6

Nomenclature

AR	cavity aspect ratio, height/width
C_f	friction coefficient
D	cavity width (m)
F	frequency (s^{-1})
F_0	reference frequency, $1/\tau_0$ (s^{-1})
f	dimensionless frequency, F/F_0
g	acceleration due to gravity (m s^{-2})
Gr	Grashof number, $g\beta qD^5/(k\nu^2) = Ra/Pr$ (–)
k	thermal conductivity (W m^{-1} K^{-1})
Nu_1	first Nusselt number, $1/T_{max}$
Nu_2	second Nusselt number, $(2/3)/\langle T\rangle$
P	pressure (N m^{-2})
p	dimensionless pressure, $P/(\rho U_0^2)$
Pr	Prandtl number, ν/α
q	power density (W m^{-3})
q''	heat flux (W m^{-2})
Ra	Rayleigh number, $g\beta qD^5Pr/(k\nu^2)$
t	dimensionless time, τ/τ_0
T	dimensionless temperature, $(\vartheta - \vartheta_w)/\vartheta_c$
U, V	velocity components (m s^{-1})
U_0	velocity scale, D/τ_0 (m s^{-1})
u, v	dimensionless velocities, U/U_0 and V/U_0
X, Y	co-ordinates (m)
x, y	dimensionless co-ordinates, X/D and Y/D

Greek symbols

α	thermal diffusivity (m^2 s^{-1})
β	thermal expansion coefficient (K^{-1})
ϑ	temperature (K)
ϑ_c	conductive temperature scale, $(qD^2)/(8k)$ (K)
ν	kinematic viscosity (m^2 s^{-1})
ρ	density (kg m^{-3})
τ	time (s)
τ_0	convective time scale, $4\pi(2/Gr)^{1/2}(D^2/\nu)$ (s)
τ_M	momentum diffusive time scale, D^2/ν (s)
Ψ	dimensionless stream function

Subscripts

c	conductive
P	periodic
w	wall
0	reference

According to the value of Gr, different flow regimes were obtained: steady-state, periodic, and chaotic. Steady-state flow, exhibiting bilateral (left–right) symmetry, was predicted for Grashof numbers up to $\sim 2 \times 10^5$. The first instability of the steady-state solution occurred at $Gr \approx 3 \times 10^5$ in agreement with the linear stability analysis conducted by Gershuni and co-workers for the limiting case of an infinitely slender cavity [6]. It was associated with the growth of an anti-symmetric velocity disturbance propagating downwards as a travelling wave with a dimensionless wave number of ~ 1 and a dimensionless propagation speed of ~ 0.2 (see Section 3 for the scales used). The resulting time-periodic flow field consisted of a central rising plume and of convection rolls, periodically generated in the upper corners of the cavity and descending regularly along the vertical isothermal walls. Transition from periodic to chaotic motion occurred at $Gr \approx 1 \times 10^6$; up to the highest Grashof numbers studied, the fluid motion exhibited a recognisable dominating frequency, associated with the process of roll renewal and scaling as $Gr^{1/2}$. The flow field still consisted of a meandering rising plume and of descending convection rolls, but these coherent structures were now irregular in shape, size and velocity.

For Grashof numbers larger than $\sim 10^6$ (chaotic flow), the friction coefficient averaged along the vertical walls was found to scale as $Gr^{-1/3}$ and the Nusselt number (overall/conductive heat transfer) as $Gr^{1/6}$.

In the present paper, a corresponding study is described for the case of a square enclosure ($AR = 1$) with the same thermal boundary conditions and for a comparable range of Grashof numbers (10^5–10^9). The computational domain and the relevant nomenclature are shown in Fig. 1. The case of a shallow enclosure ($AR = 0.25$) will be considered in a companion paper.

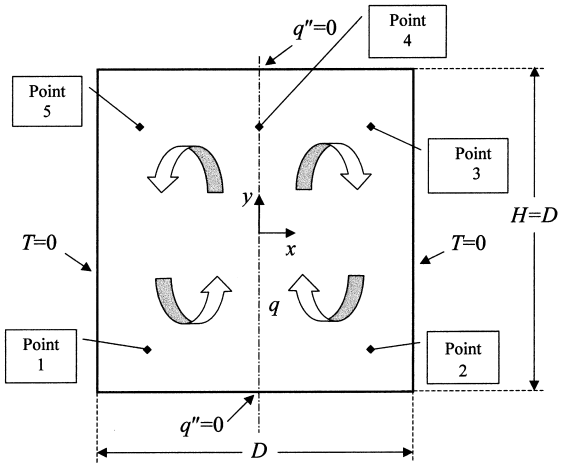

Fig. 1. Sketch of the model square cavity with isothermal vertical walls and adiabatic horizontal walls. The location of monitoring points P1–P5 is indicated.

2. Literature review

In contrast with the rich literature on the numerical computation of unsteady flows in differentially heated enclosures, published results for free convection in enclosures with internal heat generation are relatively scarce and most of them regard Prandtl numbers larger than unity; a review was given in Ref. [1].

Of particular interest here are previous computational studies dealing with square cavities. For this geometry, Churbanov et al. [7] solved the two-dimensional Navier–Stokes equations (recast in ψ–ω form) for Rayleigh numbers of 10^5–10^8 and $Pr = 7$. They tested alternative thermal boundary conditions (not including, however, those used in the present work) and obtained symmetry-breaking and time-periodic unsteady solutions. Periodic solutions were also computed by May [8] at $Ra > 3.2 \times 10^6$ for a square cavity at $Pr = 7$ with all walls isothermal.

Turbulence models, rather than direct (albeit two-dimensional) simulations, were used by other authors. Farouk [9], using the k–ε model, obtained symmetry-breaking solutions for a cavity of $AR = 0.5$ at $Pr = 6.5$ and $Ra = 2 \times 10^6$–2×10^9. Though a time-marching approach was used to compute the initial transient, the flow settled to a steady state and time dependence was not explicitly simulated due to the use of a turbulence model. Alternative turbulence models were tested and developed by Dinh and co-workers [10] with applications to corium cooling problems, but for hemispherical geometries quite far from the square one considered here.

Acharya and Goldstein [11] considered a square box arbitrarily oriented with respect to the horizontal and subjected to simultaneous internal heat generation and differential heating of two opposite walls. The Prandtl number was 0.7. They used a rather coarse grid (32×32 nodes) and conducted only steady-state simulations. Mixed (internal + external) heating was also simulated by Fusegi et al. [12] using a time-marching finite volume method on much finer grids (122×122 nodes). For the case of internal heating only and $Pr = 5.85$, they obtained steady-state and bilaterally symmetric solutions up to Rayleigh numbers of $\sim 10^{10}$ ($Gr \approx 2 \times 10^9$).

3. Model and numerical methods

As indicated in Section 1, the physical model adopted in the present study consists of a square cavity of height and width D. Fig. 1 reports the location of five monitoring points which will be used in the following. The fluid motion is driven by a uniform internal power density q, the left and right walls being at constant temperature, ϑ_w and the upper and lower boundaries at zero heat flux. The fluid considered here has a Prandtl number of 0.0321, which corresponds to a liquid metal Li–17Pb alloy at 300°C.

In order to write the governing equations in dimensionless form, appropriate scales were chosen for length, temperature, time, velocity and pressure following the approach in Ref. [1]. The length scale is the size D of the enclosure. The temperature scale is the conductive peak temperature $\vartheta_c = qD^2/(8k)$. As regards the frequency or time scales, by analogy with the Brunt–Väisälä frequency $F_{BV} = (g\beta|\partial\vartheta/\partial Y|)^{1/2}/(2\pi)$ which characterises stably stratified flows [13], the reference frequency $F_0 = (g\beta\vartheta_c/D)^{1/2}/(2\pi)$ was used. The corresponding time scale is $\tau_0 = F_0^{-1}$, which may be written as $\tau_0 = (4\pi\sqrt{2}Gr^{-1/2})\tau_M$, $\tau_M = D^2/\nu$ being the momentum diffusive time scale and $Gr = g\beta qD^5/(k\nu^2) = Ra/Pr$ the Grashof number. A velocity scale coherent with the above definitions is $U_0 = D/\tau_0$, i.e. the ratio of length to time scales. Finally, an appropriate pressure scale is ρU_0^2. As confirmed a posteriori by the computational results, the above choice of scales allowed all variables to remain of order one throughout the range of parameters investigated.

The two-dimensional continuity and momentum equations, coupled with the energy transport equation under the Boussinesq approximation, may now be written in dimensionless form as:

$$\frac{\partial u}{\partial x} + \frac{\partial v}{\partial y} = 0 \tag{1}$$

$$\frac{\partial u}{\partial t} + u\frac{\partial u}{\partial x} + v\frac{\partial u}{\partial y} = -\frac{\partial p}{\partial x} + \frac{4\pi\sqrt{2}}{\sqrt{Gr}}\left(\frac{\partial^2 u}{\partial x^2} + \frac{\partial^2 u}{\partial y^2}\right) \tag{2a}$$

$$\frac{\partial v}{\partial t} + u\frac{\partial v}{\partial x} + v\frac{\partial v}{\partial y} = -\frac{\partial p}{\partial y} + \frac{4\pi\sqrt{2}}{\sqrt{Gr}}\left(\frac{\partial^2 v}{\partial x^2} + \frac{\partial^2 v}{\partial y^2}\right) + 4\pi^2 T \tag{2b}$$

$$\frac{\partial T}{\partial t} + u\frac{\partial T}{\partial x} + v\frac{\partial T}{\partial y} = \frac{4\pi\sqrt{2}}{\sqrt{Gr}\cdot Pr}\left(\frac{\partial^2 T}{\partial x^2} + \frac{\partial^2 T}{\partial y^2} + 8\right) \tag{3}$$

in which $x = X/D$, $y = Y/D$, $u = U/U_0$, $v = V/U_0$, $p = P/(\rho U_0^2)$, $T = (\vartheta - \vartheta_w)/\vartheta_c$, $t = \tau/\tau_0$. The boundary conditions are:

$$u = v = 0, \qquad \partial T/\partial y = 0 \quad \text{for } y = \pm 1/2 \tag{4}$$

$$u = v = 0, \qquad T = 0 \quad \text{for } x = \pm 1/2 \tag{5}$$

The range of Grashof numbers investigated was from 10^5 to 10^9. For $Gr < 10^5$, convection plays a negligible

role, while for $Gr > 10^9$, the explicit resolution of all energy containing spatial and temporal features of the flow would require prohibitive computational grids and computing times.

Eqs. (1)–(3) were solved by using a finite-volume technique based on the SIMPLEC pressure–velocity coupling algorithm [14], Crank–Nicholson time stepping and the central discretisation scheme for both diffusion and advection terms. Details are discussed in Ref. [1].

As will be discussed in the following sections, according to the Grashof number, the flow either attained a steady-state configuration or exhibited periodic or chaotic unsteadiness. In the former case ($Gr \leq 3 \times 10^7$), the simulation was protracted until no significant variation of monitored quantities was observed. This typically required 5–25 time constants τ_0 (defined above), the larger time being necessary for the case $Gr = 3 \times 10^7$ which exhibited spatial symmetry breaking.

In the cases with time-dependent behaviour, the flow exhibited recognisable lowest frequencies ranging from $\sim 2.4/\tau_0$ (periodic flow obtained at $Gr = 5.4 \times 10^7$) to $\sim 0.3/\tau_0$ (chaotic flow at $Gr = 10^8$). Simulations were protracted in each case so as to include many corresponding periods, i.e. for a dimensionless time of ~5–15. One time unit τ_0 was typically resolved by 400 time steps.

Computational grids ranged from 80 × 80 nodes ($Gr < 10^8$) to 128 × 128 nodes ($Gr = 10^8$ and 10^9), and were selectively refined near the walls by using a hyperbolic tangent distribution. Grid-independence tests were conducted for the case $Gr = 10^8$ and no significant difference in time-averaged quantities and variances was observed as the grid size increased from 64 × 64 to 128 × 128. A more detailed discussion of the grid and time-step requirements for similar simulations was given in Ref. [1].

4. Results: steady-state flow

For $Gr \leq 10^7$, the flow settles to a steady-state solution possessing bilateral symmetry. The initial rate of temperature rise in the cavity is the same at all points, and is given — in dimensionless terms — by $\partial T/\partial t = (32\pi\sqrt{2})/(Pr\sqrt{Gr})$, as can be deduced from Eq. (3) for initially negligible convection and diffusion. Therefore, in the dimensionless form used here, the initial temperature slope decreases as Gr increases. At steady state, maximum temperatures are largest for the case $Gr = 10^6$, for which the conductive peak value is exceeded by ~8%. On the other hand, volume-averaged temperatures decrease monotonically with Gr; at $Gr = 10^7$, they are ~28% lower than the purely conductive value (which is 2/3 in dimensionless form),

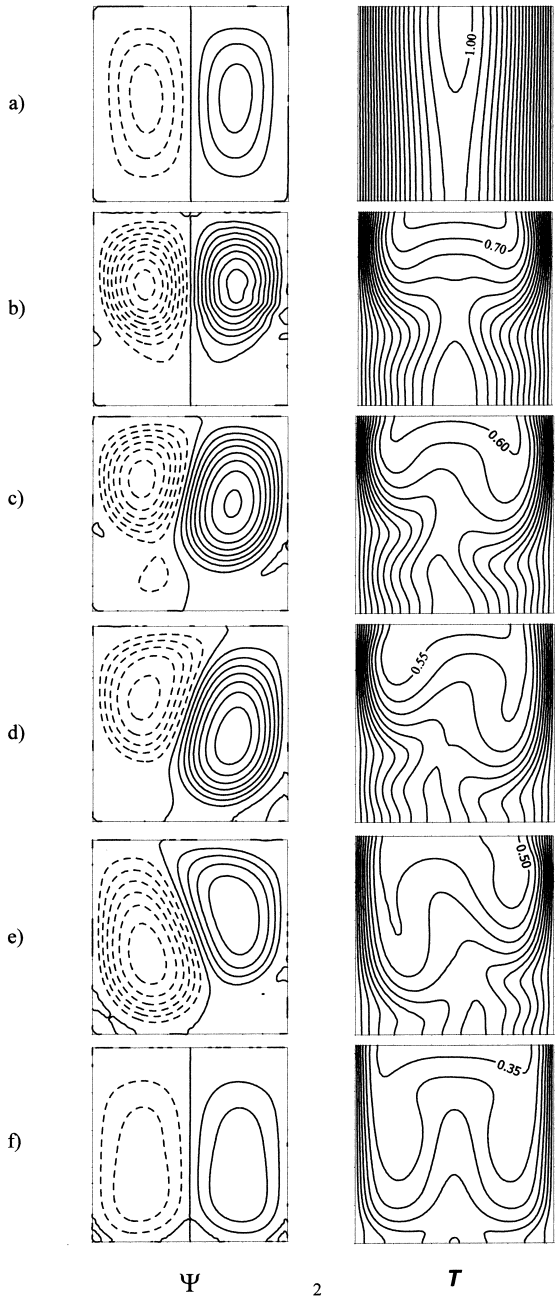

Fig. 2. Steady-state or time-averaged flow and temperature fields. Left: streamlines, dimensionless separation = 0.1 (solid lines: clockwise flow; broken lines: anti-clockwise flow). Right: isotherms, dimensionless separation = 0.05. (a) $Gr = 10^5$; (b) $Gr = 10^7$; (c) $Gr = 3 \times 10^7$; (d) $Gr = 5.4 \times 10^7$; (e) $Gr = 10^8$; (f) $Gr = 10^9$.

while at the lowest Gr (10^5), they are barely distinguishable from the conductive value, which indicates that convection contributes little to heat transport at

such a low Gr, at least for the present Prandtl number (0.0321).

Steady-state dimensionless stream function Ψ and temperature T are shown in Fig. 2a and b for $Gr = 10^5$ and 10^7. The stream function is made dimensionless with respect to $DU_0 = D^2/\tau_0$. Results are qualitatively similar to those previously obtained for a slender cavity of $AR = 4$ [1]; there is only one circulation cell in each half of the enclosure, with a perfect bilateral symmetry. The case at the lowest Gr (10^5) also exhibits roughly top–bottom symmetry in Ψ and mainly horizontal stratification in T, due to the dominant role played by conduction. At higher Gr, the role of convection increases and a moderate vertical thermal stratification develops, especially in the upper region of the enclosure.

For a Grashof number of 3×10^7, a markedly different behaviour was predicted. Fig. 3 reports dimensionless velocities as functions of time at the monitoring points P1–P2 and P3–P5 (symmetrically located with respect to the vertical centreline). After $t \approx 5$, the flow tends to a symmetric steady state. However, full convergence to this configuration is never attained, and for $t \approx 10$, quantities related to spatially symmetric points begin to diverge until, at $t \approx 20$, an asymmetric steady state is attained. The evolution of the flow field from the initial state of still fluid to the final asymmetric configuration, through intermediate symmetric states, is better shown in Fig. 4 in the form of vector plots of the instantaneous velocity at regular intervals of ~ 2.8 (in τ_0 units).

The final, steady-state, stream function and temperature distributions are shown for this case in Fig. 2(c). The temperature field, as compared with that computed for the last symmetric case at $Gr = 10^7$ (Fig. 2(b)) exhibits only a slight reduction of the maximum value (from ~ 0.7 to ~ 0.6 in dimensionless terms), but shows a significant asymmetric distortion of the whole distribution.

The transition from symmetric to asymmetric steady states indicates the existence of a pitchfork bifurcation, with spatial symmetry breaking, at some intermediate value of Gr between 10^7 and 3×10^7. A similar symmetry breaking was predicted by Churbanov et al. [7] for a square box at $Pr = 7$ and $Gr \approx 10^7$, and by Farouk [11] for $AR = 0.5$, $Pr = 6.5$, $Gr \approx 10^7$, but not by Fusegi [10] for $AR = 1$, $Pr = 5.85$ and Grashof numbers up to $\sim 10^9$.

5. Results: periodic flow

For a Grashof number of 5.4×10^7 (midway between 3×10^7 and 10^8 in a logarithmic scale), a perfectly time-periodic solution was predicted. Fig. 5 reports the time-dependent behaviour of vertical velocities v at the monitoring points P1–P2 and P3–P5 (symmetric with respect to the vertical centreline). Following an initial transient — quite similar to that observed for the symmetric steady-state case $Gr = 10^7$ — at $t \approx 15$, fluctuations start to develop in all quantities and result in regular periodic oscillations at $t \approx 25$. Since periodic oscillations develop further to the spatial symmetry breaking (which occurs at $t \approx 10$),

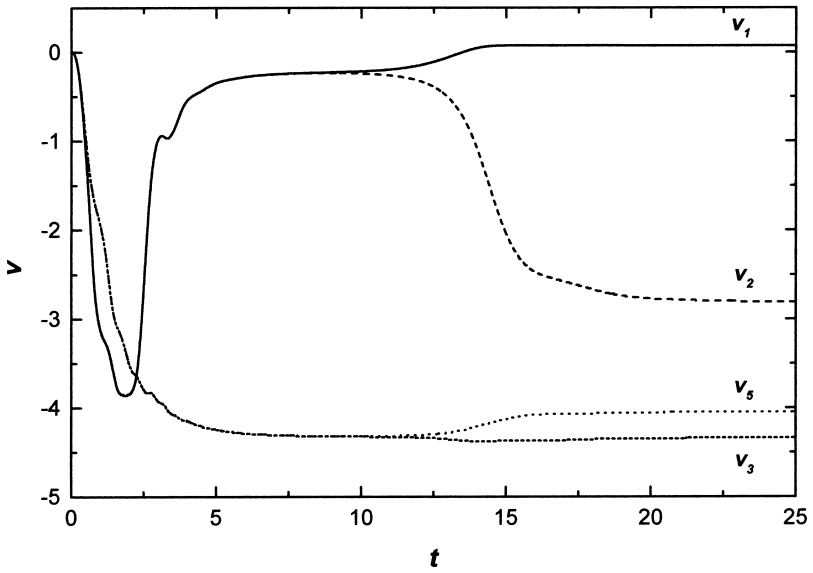

Fig. 3. Predictions for the case $Gr = 3 \times 10^7$, attaining an asymmetric steady-state condition: dimensionless vertical velocity v at monitoring points P1–P2 and P3–P5, symmetrically located with respect to the centreline $x = 0$.

they are superimposed on a base flow which is already spatially asymmetric with respect to the cavity vertical centreline.

Instantaneous vector plots during the initial transient, up to the onset of periodic oscillations, show symmetry breaking like Fig. 4 and are not reported here. After periodicity has been attained, the period of the oscillation is ~0.42 (τ_0 units), corresponding to a dimensionless frequency of ~2.4. The behaviour of the flow field, as indicated by vector plot animations of the fluctuating velocity, can be interpreted as due to the passage of an anti-symmetric velocity disturbance which moves upward as a travelling wave with vertical wavelength ~2/3 and propagation speed ~1.6 (in the present dimensionless form), so as to yield a dimensionless frequency of ~2.4. Further complexities are

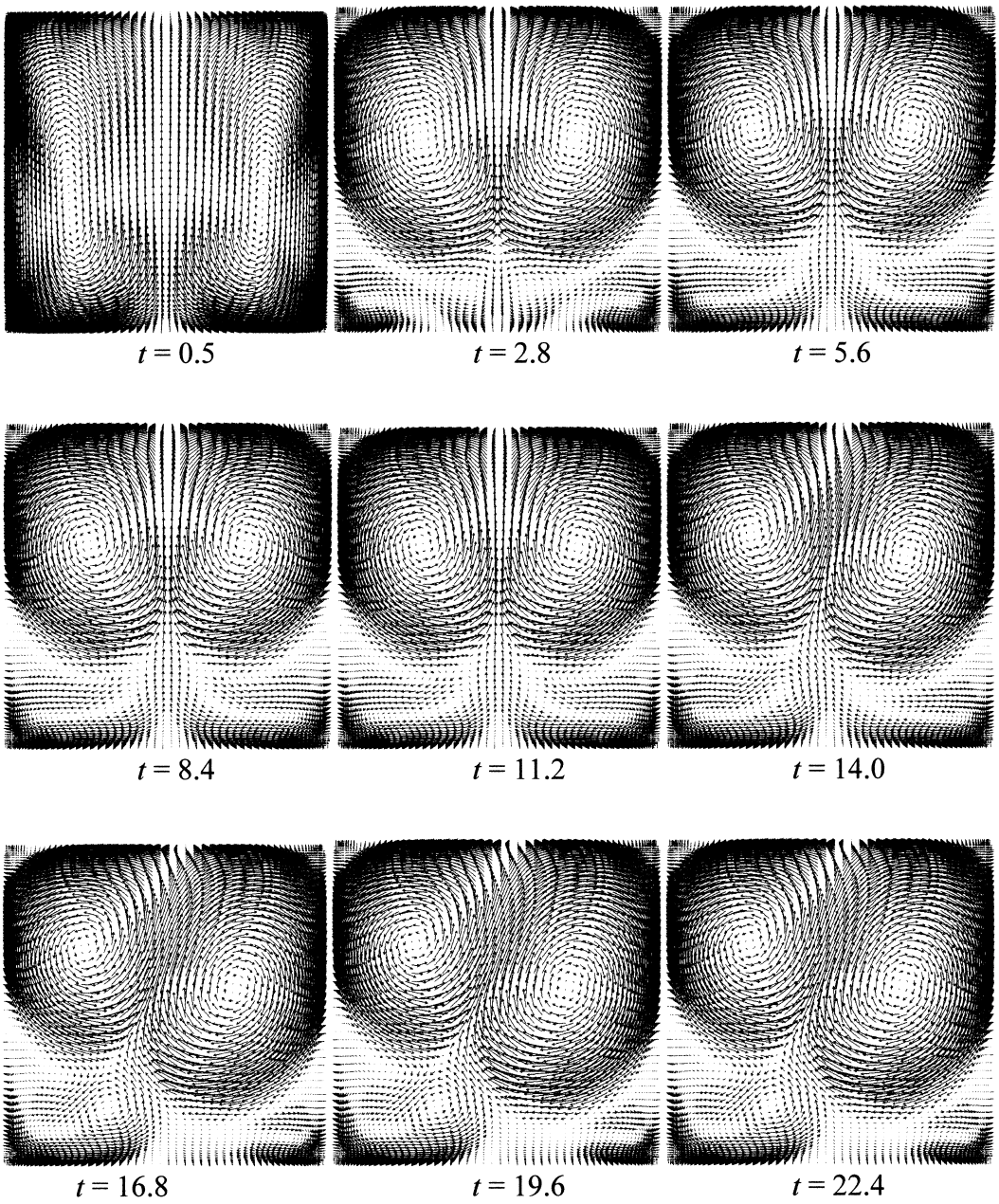

Fig. 4. Evolution of the flow field to the final asymmetric steady state for $Gr = 3 \times 10^7$. Frames 2–9 are at regular intervals of 2.8 τ_0 units.

introduced by the presence of the horizontal walls and by the anti-symmetric nature of the base steady-state flow. In the overall (mean + fluctuating) flow, the periodic time dependence is barely observable due to the small amplitude of the oscillations, and appears as a cyclic motion of the roll centres around small, roughly elliptic, orbits.

Power spectra of the dimensionless vertical velocity v and temperature T at any monitoring point, computed from the sequences in Fig. 5 using data in the interval $t = 25$–30 (which covers roughly 12 periods), show a sharp peak at $f \approx 2.4$; the only other significant peak corresponds to the first harmonic of the above periodic frequency ($f \approx 4.8$).

Time-averaged distributions of the dimensionless stream function and temperature for the present periodic case at $Gr = 5.4 \times 10^7$ are reported in Fig. 2(d). The asymmetry of the time-averaged flow and temperature fields can be observed; the maximum dimensionless temperature is ~ 0.55.

6. Results: chaotic flow

The periodic flow in the present cavity exists only in a narrow range of Grashof number, as was the case for the slender cavity of aspect ratio 4 [1]. For $Gr = 10^8$, perfect time periodicity is already lost and irregular fluctuations begin to appear in the flow and temperature field.

Fig. 6 reports the dimensionless vertical velocity v at the monitoring points P1 and P2 as a function of time, and can be compared with Fig. 5 (relative to the periodic flow at $Gr = 5.4 \times 10^7$). In the present case, spatial symmetry breaking occurs at a comparable dimensionless time ($t \approx 13$), but is accompanied without any significant delay by the growth of irregular oscillations.

A normalised power spectrum is reported in Fig. 7(a) for the vertical velocity v at monitoring point 1. It was obtained by processing the corresponding time series between $t = 27$ and $t = 42$ (τ_0 units). The subharmonic frequency $f \approx 0.27$ is clearly visible, and its amplitude even exceeds that associated with the pseudo-periodic frequency f_P. The spectrum exhibits, quite close to the pseudo-periodic frequency $f_P \approx 2$, a lower frequency of ~ 1.7. The highest value of f still associated with a significant energy content is ~ 4. Although other frequencies are present, it can be stated that the flow is characterised by just three main unrelated frequencies (0.27, 1.7, and 2), suggesting that the present Grashof number of 10^8 is close to a quasi-periodic condition and is probably just beyond the critical value for transition to proper chaotic behaviour. The existence of intermediate quasi-periodic regimes is difficult to ascertain merely by numerical simulations, but could be the subject of future analysis.

Time-averaged distributions of the dimensionless stream function and temperature for $Gr = 10^8$ are reported in Fig. 2(e). The asymmetry of both the flow and the temperature fields can be observed; results, apart from the opposite parity, are similar to those

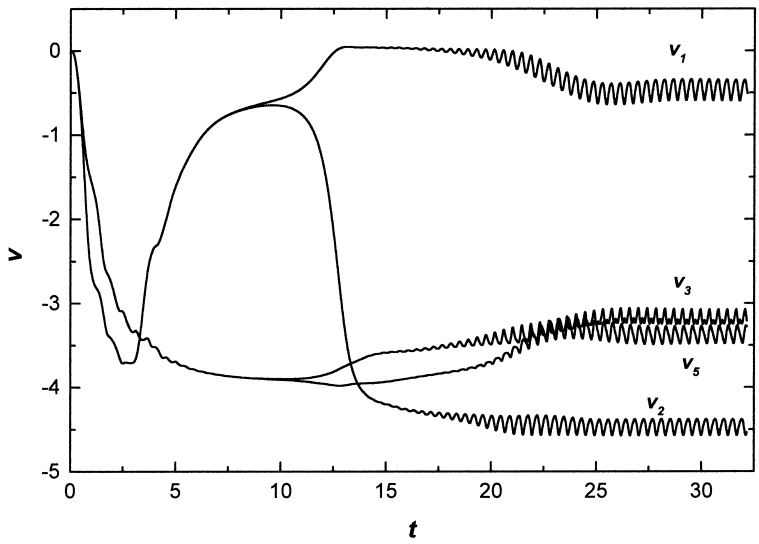

Fig. 5. Predictions for the periodic case $Gr = 5.4 \times 10^7$: dimensionless vertical velocity v at monitoring points P1–P2 and P3–P5, symmetrically located with respect to the centreline $x = 0$.

reported in Fig. 2(d) for the periodic case $Gr = 5.4 \times 10^7$. The maximum dimensionless temperature is slightly lower (~0.5).

The further increase of the Grashof number to 10^9 leads to a fully chaotic behaviour, in which the left–right asymmetry observed for the previous cases is lost and time averages exhibit an almost perfect bilateral symmetry. The time evolution of the dimensionless velocity v at monitoring points P1 and P2 is shown in Fig. 8 for an overall duration of ~35 τ_0 units. The highly irregular behaviour of all quantities, and the disappearance of any marked asymmetry between the left and right halves of the enclosure in the long-term behaviour of the flow, can be observed. Quantities relative to spatially symmetric points initially exhibit identical, though apparently chaotic, oscillations, and begin to diverge at a dimensionless time of ~10, close to that observed for the previous asymmetric flows at $3 \times 10^7 \leq Gr \leq 10^8$. However, in the present case, large irregular oscillations develop simultaneously and prevent the flow from settling to an asymmetric base pattern.

A normalised power spectrum (derived from the interval $t = 20$–35) is shown in Fig. 7(b) for the vertical velocity v at the monitoring point P1. The dominant frequency is $f_P \approx 0.8$ and is associated with the most conspicuous fluctuations of the vertical velocity v in Fig. 8; it corresponds to the pseudo-periodic frequency of ~2 observed for the previous case at $Gr = 10^8$, Fig. 7(a), and to that of ~2.4 observed for the periodic case at $Gr = 5.4 \times 10^7$.

The symmetric nature of the time-averaged flow and temperature distributions is evidenced in Fig. 2(f). The significant reduction of the dimensionless temperature maximum from 0.5 to 0.35 as Gr increases by an order of magnitude can be observed. Streamlines show that time-mean circulation centres are now located close to the bottom of the cavity.

7. Shear stress and heat transfer

Fig. 9(a) reports time-averaged profiles of the wall shear stress along the side walls for all the cases studied. The wall shear stress was further averaged between the left and right walls and normalised by ρU_0^2, thus taking the form of a friction coefficient C_f. All curves exhibit a peak near the cavity top, where the horizontal boundary layers turn and meet the cold walls. Top–down asymmetry is low for the case at lowest Gr (10^5), when the role of convection is marginal and also the flow field is roughly top–down symmetric. Maximum local values of C_f (~3), and the largest top–down asymmetry, are attained for the following case $Gr = 10^6$, while peaks of C_f decrease, and its profile become more uniform, as Gr increases further. C_f is low (~0.2) and rather uniform along the walls for the fully chaotic case $Gr = 10^9$.

Separate profiles of C_f along the left and right walls are reported in Fig. 9(b) for the asymmetric cases $Gr = 3 \times 10^7$ (steady state), 5.4×10^7 (periodic), and 10^8 (chaotic) in order to evidence the degree of asymmetry

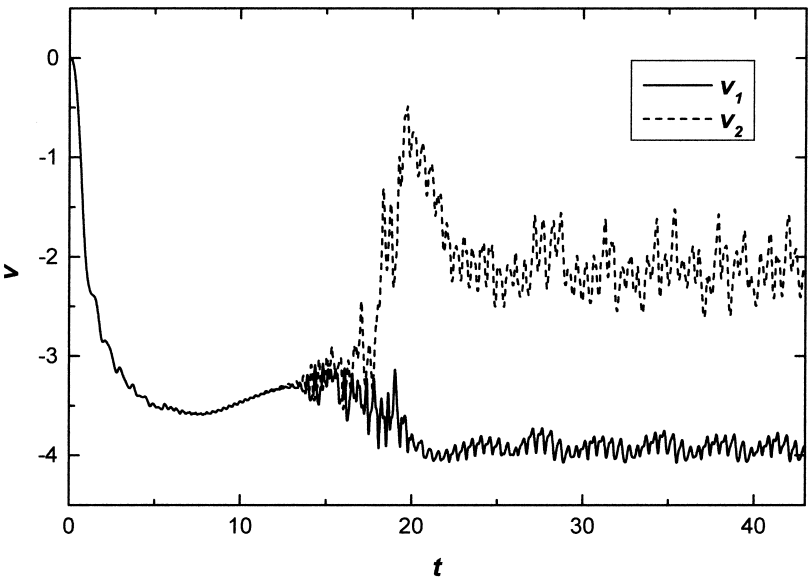

Fig. 6. Predictions for the early chaotic case $Gr = 10^8$: dimensionless vertical velocity v at monitoring points P1–P2, symmetrically located with respect to the centreline $x = 0$.

in the wall friction coefficient associated with the asymmetry of the bulk flow.

Fig. 10 reports $\langle C_f \rangle$, i.e. the spatially averaged value of C_f, as a function of Gr over the whole range studied. At the lowest values of the Grashof number (10^5), the computed value of $\langle C_f \rangle$ approaches a limiting value of $\sim$1.7, which is significantly lower than the value $4\pi^2/15 \approx 2.63$ deduced analytically in Ref. [1] for the case of parallel flow in an infinitely slender enclosure. However, it can be observed from Fig. 9(a) that the maximum of C_f (shifted upwards with respect to mid-height) is quite close to the above value, while the regions near the horizontal walls lower the average substantially. At higher Gr, $\langle C_f \rangle$ decreases roughly as $Gr^{-1/3}$, as in the case $AR = 4$ [1]. Note that as a consequence, the *dimensional* wall shear stress increases as $U_0^{4/3}$, thus exhibiting a behaviour intermediate between that of a viscous and that of a hydraulic resistance. Also note that the transition from steady to unsteady flow at $Gr \approx 3 \times 10^7$ is associated with a slight increase

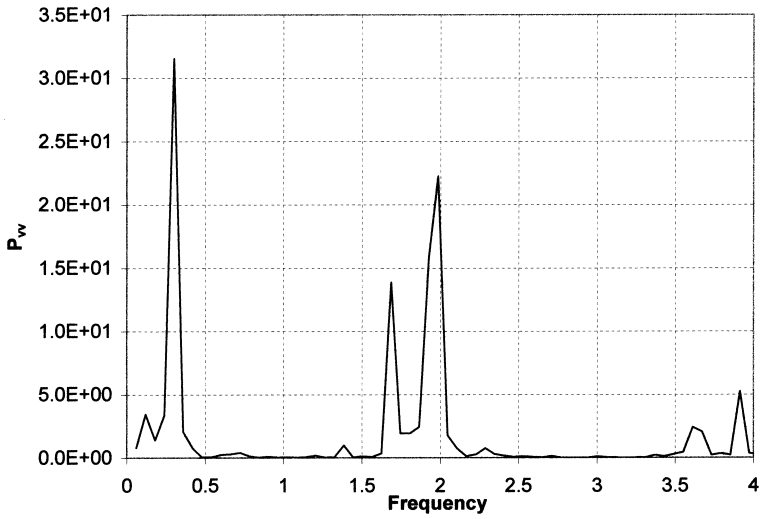

(a)

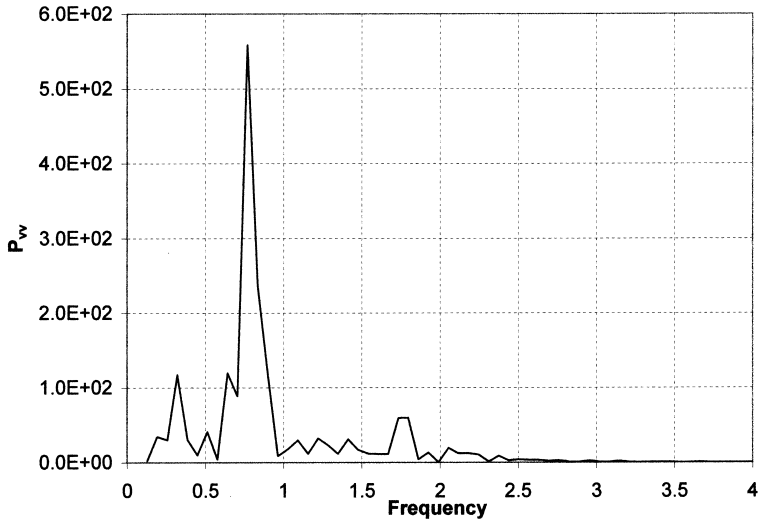

(b)

Fig. 7. Normalised power spectrum of the vertical velocity v at monitoring point P1.(a) $Gr = 10^8$ (early chaotic flow); (b) $Gr = 10^9$ (fully chaotic flow).

of $\langle C_f \rangle$, while its $(-1/3)$ power-law dependence upon Gr remains basically unchanged.

As regards heat transfer, for the present configuration the mean value of the wall heat flux under thermal equilibrium conditions is $qD/2$; this value can be used to normalise the local and/or instantaneous values of the wall heat flux q''.

Fig. 11(a) reports the wall heat flux profiles for all the cases studied; for the time-dependent cases, all curves represent long-term time averages and were further averaged between the left and right walls to cancel the effect of the flow asymmetry (if present). At low Gr (10^5 and, partly, 10^6), the curves are quite flat, with small variations with respect to their mean value. On the other hand, large variations are present for higher Grashof numbers, especially in the chaotic range. Peak values of ~1.6–1.7 are obtained in correspondence with the impingement of hot fluid on the cold walls near the cavity top, while lowest values correspond to the separation of the wall boundary layers near the cavity bottom. For the present aspect ratio of 1, the central region of the cavity does *not* exhibit a flat distribution of q'' as occurred in a slender enclosure of $AR = 4$ [1].

Separate profiles of the normalised heat flux along the left and right walls are reported in Fig. 11(b) for the asymmetric cases $Gr = 3 \times 10^7$ (steady state), 5.4×10^7 (periodic), and 10^8 (chaotic) in order to evidence the effect of the flow asymmetry on wall heat transfer.

Finally, the influence of Gr on overall heat transfer is shown in Fig. 12. This reports the quantities $Nu_1 = 1/T_{max}$ (T_{max} being the time-averaged maximum temperature in the cavity) and $Nu_2 = (2/3)/\langle T \rangle$ ($\langle T \rangle$ being the time- and space-averaged temperature). This latter definition is such that it gives $Nu_2 = 1$ for a purely conductive temperature distribution. Both quantities can be regarded as alternative definitions of the Nusselt number (ratio of overall to conductive heat transfer) for the present configuration. They are plotted as functions of the Grashof number, showing results from all the cases examined.

It is interesting to observe that for Grashof numbers below 10^7 (corresponding to steady-state, symmetric flow), convection actually results in an *increase* of the temperature maximum ($Nu_1 < 1$) by transporting hot fluid into the hottest region of the enclosure (adjacent to the top adiabatic wall). A similar result was obtained for the case of a slender enclosure [1] for Gr up to 2×10^6, and was also observed by de Socio et al. [15] in correspondence with transitional values of Gr for internally heated cavities

As expected in liquid metals, Nu_1 and Nu_2 never become very high, attaining a common value of about 2.66 at the highest Gr (10^9). This is similar to the values obtained for the slender enclosure [1] (~2.4–2.7 for Nu_1 and Nu_2, respectively) at the slightly higher Gr of 1.26×10^9, which shows that the Nusselt number scales well with the Grashof number based on the cavity *width* rather than on its height. Note that in the present case of a square enclosure, strong vertical mixing suppresses any significant vertical thermal stratification and causes the above two definitions of the Nusselt number, practically, to coincide at $Gr \geq 3 \times 10^7$ (unsteady flow). On the contrary, for $AR = 4$, Nu_1 and

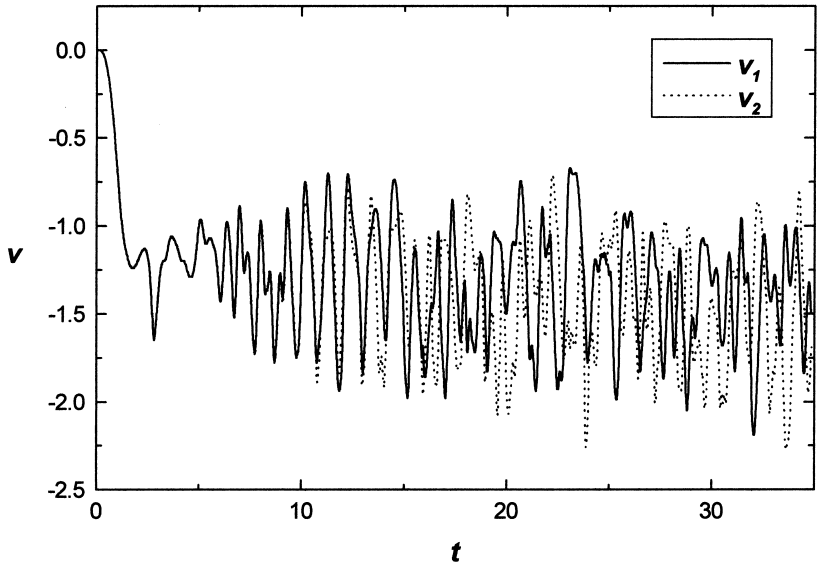

Fig. 8. Predictions for the fully chaotic case $Gr = 10^9$: dimensionless vertical velocity v at monitoring points P1–P2, symmetrically located with respect to the centreline $x = 0$.

Nu_2 were still significantly different at the highest Gr [1].

For $Gr > \sim 10^6$, both Nu_1 and Nu_2 increase approximately as $Gr^{1/7}$. This behaviour is similar to that computed for the case of a slender enclosure [1] but differs from that ($Nu_2 \sim Gr^{0.23-0.24}$) indicated by the experimental results of Fiedler and Wille [16] and Kulacki and Nagle [17] and by the computational studies of Farouk [9] and Dinh and Nourgaliev [10], which, however, refer to shallow layers cooled only from the upper surface and to a Prandtl number of 6–7. The lower Grashof number dependence found in the pre-

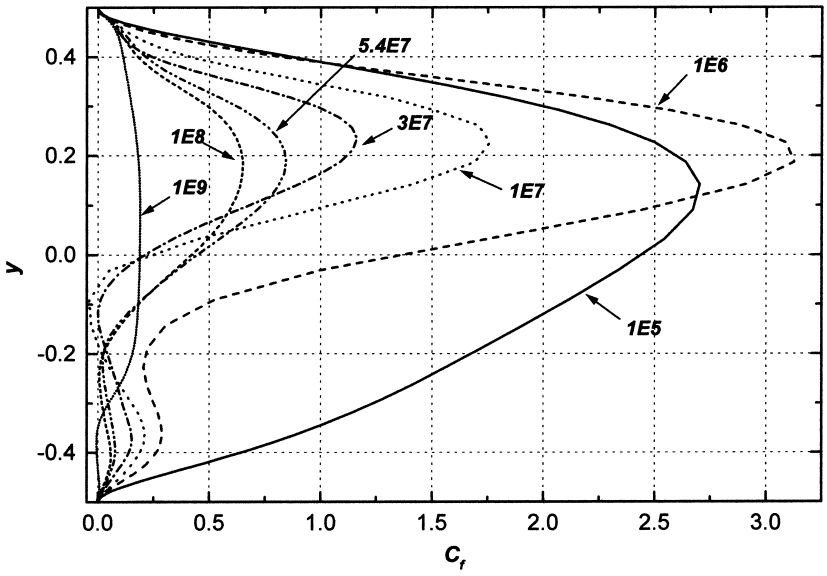

(a)

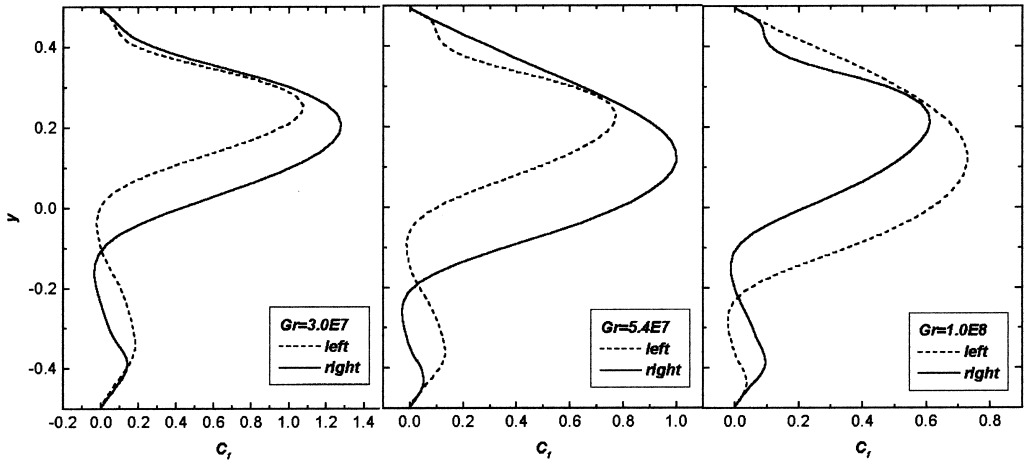

(b)

Fig. 9. Steady-state or time-averaged friction coefficient. (a) Profiles of C_f along the vertical walls for the all cases investigated. For the asymmetric cases, the mean of left and right wall values is shown. (b) Separate profiles of C_f along left and right walls for the asymmetric cases.

sent study is justified by the lower Prandtl number considered (0.0321).

8. Conclusions

Numerical predictions of the flow and temperature fields in an internally heated square enclosure at $Pr = 0.0321$ and $Gr = 10^5$–10^9 indicate the existence of a pitchfork bifurcation, with spatial symmetry breaking, at $10^7 < Gr < 3 \times 10^7$; of a Hopf bifurcation to periodic flow at $3 \times 10^7 < Gr < 5.4 \times 10^7$; and of a final transition to chaotic flow at $5.4 \times 10^7 < Gr < 10^8$, probably passing through an intermediate range of quasi-periodic flow. The transition from steady to unsteady flow occurs at a comparable Grashof number, based on the cavity *height*, for the slender and the square enclosures. The mechanisms of transition, however, appear to be considerably different.

As summarised in Section 1, for the previously studied case of a slender cavity of $AR = 4$ [1] transition to time-periodic flow regimes occurred at $Gr \approx 3 \times 10^5$ and was associated — in agreement with the linear stability results of Gershuni and co-workers [6] — with the growth of a travelling wave anti-symmetric disturbance of the base flow, propagating downward with a dimensionless wavelength ~1 and a celerity ~0.2. In the present case, the steady but spatially asymmetric flow occurring at $Gr \approx 1 \sim 3 \times 10^7$ can be regarded — at some distance away from the top and bottom walls — as the superposition of a symmetric steady base flow, similar to that computed for the slender cavity, and of an anti-symmetric steady disturbance (stationary-wave) of vertical wavelength ~1 (in the present dimensionless formulation based on D) and appropriate amplitude. The latter disturbance is similar, apart from its zero propagation speed, to that responsible for the Hopf bifurcation in the slender cavity. In its turn, the time-dependent flow established in the present case at $Gr > \sim 5 \times 10^7$ can be interpreted as the further superposition on the above steady asymmetric flow of an anti-symmetric travelling wave disturbance of comparable vertical wavelength (~2/3), but propagating *upward* with higher speed (~1.6). Therefore, the time-dependent flow occurring in the present configuration is due to different mechanisms than that observed for the slender cavity and is, in fact, characterised by a quite different dimensionless frequency (~2.4 against ~0.2–0.3).

An open issue is the influence of the Prandtl number on flow stability and flow patterns. The infinite-AR linear stability analysis by Gershuni and co-workers [6] predicts that as Pr increases, the critical Grashof number Gr_c for the onset of periodic convection decreases while the corresponding critical Rayleigh number $Ra_c = Gr_c \times Pr$ increases, but clearly is not applicable to low aspect ratio enclosures, as the present paper shows. Numerical results for differentially heated square cavities [18] indicate that a Hopf bifurcation to time-periodic flow occurs at a critical Rayleigh number for $Pr < \sim 2$, while direct transition to chaotic flow occurs for larger values of Pr; but, again, cannot be directly extended to the present internally heated configuration. Further computational studies repeated for different values of the Prandtl number will be necessary in order to clarify this issue.

It should be stressed that directly comparable results, either experimental or computational, are not available in the literature for comparison and validation of the present findings. However, the conditions

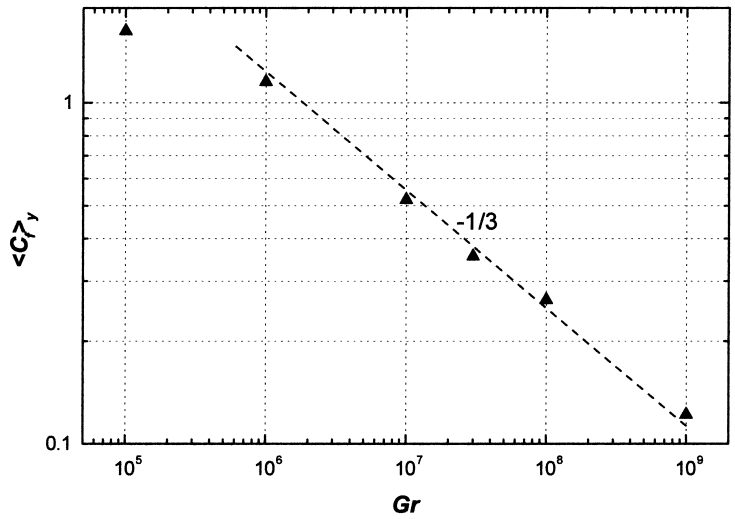

Fig. 10. Spatially averaged friction coefficient $\langle \bar{C}_f \rangle$ as a function of Gr.

studied in the present paper should not be difficult to reproduce in experiments (apart, of course, from three-dimensional and end-wall effects). For example, in a 5 × 5 cm rectangular enclosure filled with mercury ($Pr = 0.027$, very close to that considered in the present study), a Grashof number of 10^8 corresponds to a volumetric heat density of ~22 kW m^{-3}, easily achieved by Ohmic heating. The detailed measurement of velocities in liquid metal-filled, internally heated enclosures is not practically feasible, but the recording of temperature time series at selected locations in a cavity for different Grashof numbers — certainly within reach of available experimental methods — would be sufficient to observe any transition from steady symmetric to asymmetric, time-periodic and chaotic regimes. Also the measurement of the local

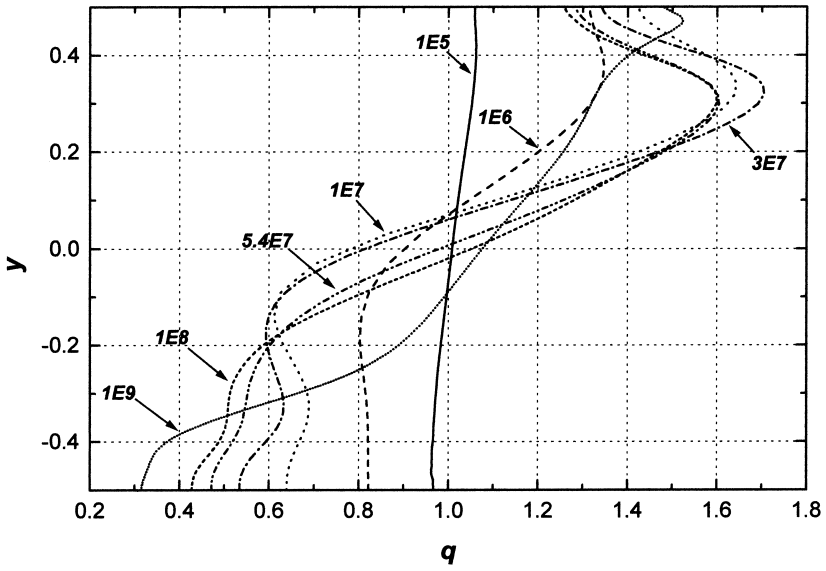

(a)

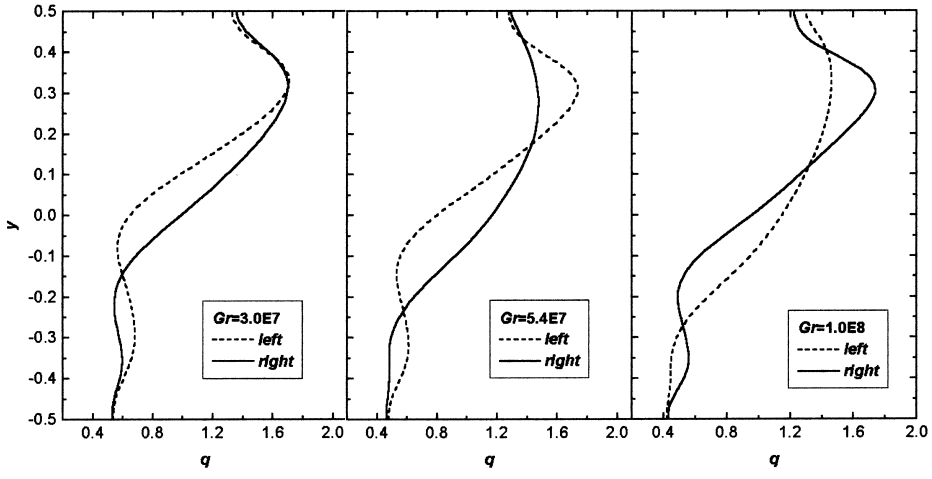

(b)

Fig. 11. Steady-state or time-averaged heat transfer quantities. (a) Profiles of the wall heat flux q'' (normalised by its mean value $qD/2$) along the vertical walls for all the cases investigated. For the asymmetric cases, the mean of left and right wall values is shown. (b) Separate profiles of q'' along the left and right walls for the asymmetric cases.

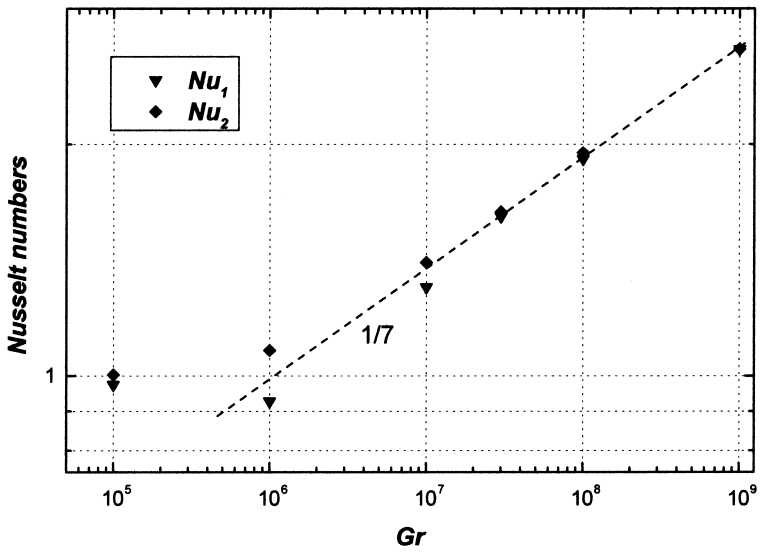

Fig. 12. Dependence of the Nusselt numbers Nu_1 and Nu_2 upon the Grashof number.

heat flux along the active walls should be experimentally feasible and would contribute to validate the present numerical, two-dimensional predictions.

References

[1] I. Di Piazza, M. Ciofalo, Low Prandtl number natural convection in volumetrically heated rectangular enclosures I. Slender cavity, $AR = 4$, Int. J. Heat Mass Transfer 43 (2000) 3027–3051.

[2] D.J. Tritton, M.N. Zarraga, Convection in horizontal layers with heat generation. Experiments, J. Fluid Mechanics 30 (1967) 21–32.

[3] E.L. Gluekler, L. Baker Jr., Post-accident heat removal in LMFBR's, in: O.C. Jones Jr., S.G. Bankoff (Eds.), Proc. Symp. on the Thermal and Hydraulic Aspects of Nuclear Reactor Safety, Liquid Metal Fast Breeder Reactors, vol. 2, ASME, New York, 1977, pp. 285–324.

[4] E. Proust, L. Anzidei, G. Casini, M. Dalle Donne, L. Giancarli, S. Malang, Breeding blanket for DEMO, Fusion Engng. and Des. 22 (1993) 19–33.

[5] W. Gudowski (Ed.), The Status of Accelerator-Driven Systems (ADS), IAEA, Vienna, 1999.

[6] F.A. Kulacki, D.E. Richards, Natural convection in plane layers and cavities with volumetric energy sources, in: S. Kakaç, W. Aung, R. Viskanta (Eds.), Natural Convection — Fundamentals and Applications, Hemisphere, New York, 1985, pp. 179–254.

[7] A.G. Churbanov, P.N. Vabishchevich, V.V. Chudanov, V.F. Strizhov, A numerical study of natural convection of a heat generating fluid in rectangular enclosures, Int. J. Heat Mass Transfer 37 (1994) 2969–2984.

[8] H.O. May, A numerical study on natural convection in an inclined square enclosure containing internal heat sources, Int. J. Heat Mass Transfer 34 (1991) 919–928.

[9] B. Farouk, Turbulent thermal convection in an enclosure with internal heat generation, Trans. ASME, Ser. C (J. Heat Transfer) 110 (1988) 126–132.

[10] T.N. Dinh, R.R. Nourgaliev, Turbulence modelling for large volumetrically heated liquid pools, Nucl. Engng. and Des. 169 (1997) 131–150.

[11] S. Acharya, R.J. Goldstein, Natural convection in an externally heated vertical or inclined square box containing internal energy sources, ASME J. of Heat Transfer 107 (1985) 855–866.

[12] T. Fusegi, J.M. Hyun, K. Kuwahara, Numerical study of natural convection in a differentially heated cavity with internal heat generation: effects of the aspect ratio, ASME J. Heat Transfer 114 (1992) 773–777.

[13] M. Lésieur, Turbulence in Fluids, Kluwer Academic Publishers, Amsterdam, 1990.

[14] J.R. van Doormal, G.D. Raithby, Enhancements of the SIMPLE method for predicting incompressible flows, Numer. Heat Transfer 7 (1984) 147–163.

[15] L.M. de Socio, L. Misici, A. Polzonetti, Natural convection in heat generating fluids in cavities, ASME Paper 79-HT-95, 1979.

[16] H. Fiedler, R. Wille, Wärmetransport bie frier Konvektion in einer horizontalen Flussigkeitsschicht mit Volumenheizung, Teil 1: Integraler Wärmetransport, in: Rep. Dtsch Forschungs- Varsuchsanstalt Luft-Raumfahrt, Inst. Turbulenzfenschung, Berlin, 1971.

[17] F.A. Kulacki, M.E. Nagle, Natural convection in a horizontal fluid layer with volumetric energy sources, ASME J. Heat Transfer 91 (1975) 204–211.

[18] C.J. Janssen, R.A.W. Henkes, Influence of Prandtl number on instability mechanisms and transition in a differentially heated square cavity, J. Fluid Mechanics 290 (1995) 319–344.